

Moiré modulation of bulk electronic structures in Cu_xTiSe_2 -based mixed two- and three-dimensional heterostructures

Renzhe Li,^{1,*} Yiwei Li,^{1,*} Shihao Zhang,^{2,*} Shenghao Dai,¹ Lixuan Xu,³ Hao Zhong,¹ Qiang Wan,¹ Chunlong Wu,¹ Cao Peng,¹ Keming Zhao,¹ Shangkun Mo,¹ Dingkun Qin,¹ Shuming Yu,¹ Xingzhe Wang,¹ Yimin Xiong,^{4,5} and Nan Xu^{1,6,†}

¹*Institute for Advanced Studies, Wuhan University, Wuhan 430072, China*

²*School of Physics and Electronics, Hunan University, Changsha 410082, China*

³*Department of Physics, Hubei University, Wuhan 430062, China*

⁴*School of Physics and Optoelectronics Engineering, Anhui University, Hefei 230601, China*

⁵*Hefei National Laboratory, Hefei 230028, China*

⁶*Wuhan Institute of Quantum Technology, Wuhan 430206, China*



(Received 17 March 2024; revised 24 June 2024; accepted 31 July 2024; published 26 August 2024)

Moiré superlattices provide a striking tool to controllably engineer electronic structures and realize various exotic quantum phenomena in two-dimensional (2D) systems. Surprisingly, moiré potential has recently been reported to extend its influence into three-dimensional (3D) graphitic thin films. Here, using angle-resolved photoemission spectroscopy, we report that 3D electronic states of transition-metal dichalcogenides (TMDs) can be modulated by interfacial moiré potential. The bulk electronic states of Cu_xTiSe_2 unambiguously exhibit moiré clones due to the lattice mismatch with the noble-gas monolayer atop. We demonstrate that the interfacial moiré effect strongly couples with charge ordering with 3D wave vectors, which plays an important role in the formation of the mixed-dimensional moiré effect. We further exclude the final-state diffraction mechanism for the observed replicas. The moiré period can be further *in situ* tuned by different noble-gas atoms and annealing temperatures. Our results broaden the horizon of the mixed-dimensional moiré family from graphitic systems to TMD-based heterostructures and shed light on constructing functional devices based on versatile 2D-3D mixed-dimensional heterostructures.

DOI: [10.1103/PhysRevB.110.085148](https://doi.org/10.1103/PhysRevB.110.085148)

I. INTRODUCTION

The periodic arrangement of atoms in crystals determines their fundamental properties. Modulating the periodicity of a crystal can drastically modify its quantum behavior and give rise to new states of matter. An emerging approach in this direction is the creation of moiré superlattices by artificial van der Waals assemblies of two-dimensional (2D) crystals [1] with a small twist angle [2–10] or a lattice mismatch [11–15]. This approach has enabled the tailoring of electronic properties in semimetallic graphene and semiconducting transition-metal dichalcogenides (TMDs), resulting in a series of discoveries of correlated [14,16,17] and topological phenomena [8,18]. Furthermore, a high-order moiré pattern can be realized in heterostructures with large lattice mismatch, as supercells of component layers share similar periods by designing twisted angles [19–23]. More intriguingly, in contrast to localized effects on the 2D interfaces, moiré potential extends its influence into three-dimensional (3D) graphitic systems, thus promising a new class of “mixed-dimensional” moiré materials [24,25]. However, this behavior is mediated by a standing wave of graphite electronic structure in a high magnetic field and it remains unknown whether the mixed-

dimensional moiré effect can be generalized to other layered semimetals and in a mild environment. Its interplays with other orders, such as charge-order wave and superconductivity, are still elusive.

The 1T-TiSe₂ family provides an ideal material platform for the exploration of moiré effects from low-dimensional systems to 3D systems. TiSe₂ is a well-studied layered semimetallic TMD material that hosts low electron- and hole density at its high-temperature normal phase [26]. It undergoes a 3D charge-density wave (CDW) transition below $T_{\text{CDW}} \sim 200$ K with a $2 \times 2 \times 2$ superlattice [27], possibly due to the synergistic contribution of exciton formation [28–30] and Peierls distortion [31–33]. By Cu intercalation, Cu_xTiSe_2 exhibits a superconducting phase transition with $T_{\text{C}} \sim 4$ K at the optimal doping $x = 0.08$ [34], and 3D CDW becomes incommensurate with wave vector around at $[\frac{1}{2}, \frac{1}{2}, \frac{1}{2} + \delta]$ and $T_{\text{CDW}} \sim 65$ K [35]. Cu doping changes the CDW from commensurate to incommensurate, but the out-of-plane CDW vector still exists. Ultrafast infrared laser irradiation drives a 3D-2D transition in TiSe₂, which recovers in 12 ps because interlayer coupling forces the CDW phase matching between layers [36].

In this work, we realize mixed-dimensional moiré interfaces between 3D Cu_xTiSe_2 ($x = 0$ and 0.08) single crystals and 2D noble-gas monolayers. The 3D electronic states of both superconducting $\text{Cu}_{0.08}\text{TiSe}_2$ and CDW TiSe₂ can be modulated by the interfacial moiré potential, as multiple

*These authors contributed equally to this work.

†Contact author: nxu@whu.edu.cn

replica bands generated by moiré wave vector \vec{G}_m directly observed via angle-resolved photoemission spectroscopy (ARPES). The moiré period can be *in situ* tuned from 15.8–47.1 Å, by choosing different noble-gas monolayer and annealing temperatures, correspondingly. Furthermore, we directly observe the interplay between 3D CDW and mixed-dimensional moiré effect in TiSe₂-based heterostructure, with replica bands resulting from a scattering vector of $\vec{Q} = \vec{q}_{\text{CDW}} + \vec{G}_m$. Our observations broaden the horizon of the 2D-3D mixed-dimensionality moiré to the TMD family and the case without magnetic field. It also promises applications based on moiré effects with a dimensional crossover.

II. METHODS

High-quality Cu_xTiSe₂ single crystals were synthesized by flux method as described in Ref. [34]. Photon-energy dependent ARPES measurements were performed at Dreamline BL09U and BL03U at Shanghai Synchrotron Radiation Facility, and beamline BL13U at the National Synchrotron Radiation Laboratory, Hefei. The Cu_xTiSe₂/noble-gas monolayer heterostructures were synthesized by the growth of monolayer noble gas on the clean cleavage surface of Cu_xTiSe₂ in a home-built vacuum-interconnected system and measured *in situ* with a lab-based He-lamp ARPES, with a similar method described in Ref. [20]. The thickness calibration of noble-gas layers is characterized via thickness-dependent valence-band spectra (Fig. S1 in the Supplemental Material [37]).

III. RESULTS AND DISCUSSION

We successfully synthesized the Cu_xTiSe₂/noble-gas monolayer heterostructures, and a moiré pattern is hosted in the system. The noble-gas monolayer forms a hexagonal structure with primitive vectors parallel to those of Cu_xTiSe₂, as indicated by low-energy electron diffraction patterns (Fig. S2 in the Supplemental Material [37]) and ARPES results discussed later. The small lattice-constant mismatch $\Delta a = a_{\text{gas}} - a_{\text{Cu}_x\text{TiSe}_2}$ ($a_{\text{Cu}_x\text{TiSe}_2} \sim 3.55$ Å, $a_{\text{gas}} \sim 4.17$ Å; a_{gas} depends on different noble-gas atoms and annealing process as discussed later) results in a hexagonal interfacial moiré pattern with period is given by $a_m = \frac{a_{\text{gas}} a_{\text{Cu}_x\text{TiSe}_2}}{\Delta a}$, as depicted in Fig. 1(a). In the center [A in Fig. 1(a)] and corner [B/C in Fig. 1(a)] regions of the moiré pattern, noble-gas atoms sit right above the Ti and bottom/top Se sites, respectively.

We examine the interfacial moiré modulation effect on electronic structure. To simplify the case, we first focus on Cu_{0.08}TiSe₂, in which no CDW folded bands are observed in ARPES experiments [41,42]. Consistent with previous studies, we observe 3D bulk- β electron pockets with an ellipsoidal shape centered at the *L* point [Fig. 1(b)]. As shown in Fig. 1(c), the in-plane Fermi surface (FS) taken with $h\nu = 21.2$ eV ($k_z = 5.16 \pi/c$) shows an intrinsic *C*₃ symmetry pattern, resulting from the tilting nature of 3D bulk- β pockets. Therefore, the clear k_z periodicity and *C*₃ symmetric in-plane FS unambiguously demonstrate the bulk state nature of the ARPES results.

We first focus on a krypton (Kr) monolayer deposited on Cu_{0.08}TiSe₂ (Cu_{0.08}TiSe₂/mKr) and directly observe the interfacial moiré modulation effect on 3D bulk states.

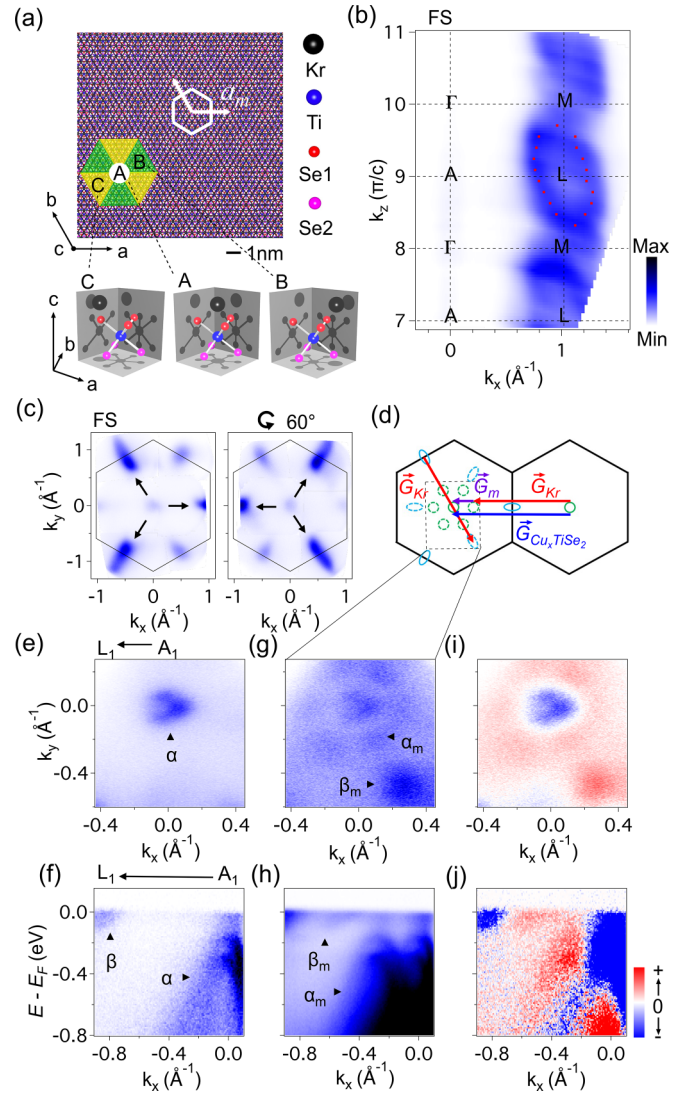


FIG. 1. Interfacial moiré effect in Cu_{0.08}TiSe₂/mKr. (a) Large-scale atom arrangements showing moiré pattern (white hexagon) in real space. Insets show a 3D view of the central (A) and corners (B and C) regions. (b) Out-of-plane Fermi surface (FS) map of Cu_{0.08}TiSe₂. The dots are extracted from band dispersions. (c) In-plane FS maps of Cu_{0.08}TiSe₂ at $k_z = 5.16 \pi/c$. Intrinsic *C*₃ symmetry of bulk states is confirmed by rotating the sample by 60°. (d) Schematic moiré effect in Cu_{0.08}TiSe₂/mKr. (e), (f) The constant energy map at $E_B = 0.15$ eV and band structure along the *A*₁–*L*₁ direction ($k_z = 5.16 \pi/c$) of Cu_{0.08}TiSe₂, respectively. (g), (h) Same as (e) and (f), but for Cu_{0.08}TiSe₂/mKr. (i), (j) FS and band-structure differences between Cu_{0.08}TiSe₂ and Cu_{0.08}TiSe₂/mKr.

Figures 1(g) and 1(h) display the constant energy map at $E_B = 0.15$ eV and band structure along the *A*₁–*L*₁ direction ($k_z = 5.16 \pi/c$) measured on Cu_{0.08}TiSe₂/mKr, respectively. Corresponding results measured on pristine Cu_{0.08}TiSe₂ are shown in Figs. 1(e) and 1(f). One can immediately recognize that apart from the holelike bands α and electron-like bands β from pristine Cu_{0.08}TiSe₂, additional holelike bands α_m and electron-like bands β_m appear along the *A*₁–*L*₁ direction in Cu_{0.08}TiSe₂/mKr, centered at $k_x = -0.3$ and -0.72 Å⁻¹, respectively. The α_m and β_m bands can be better visualized

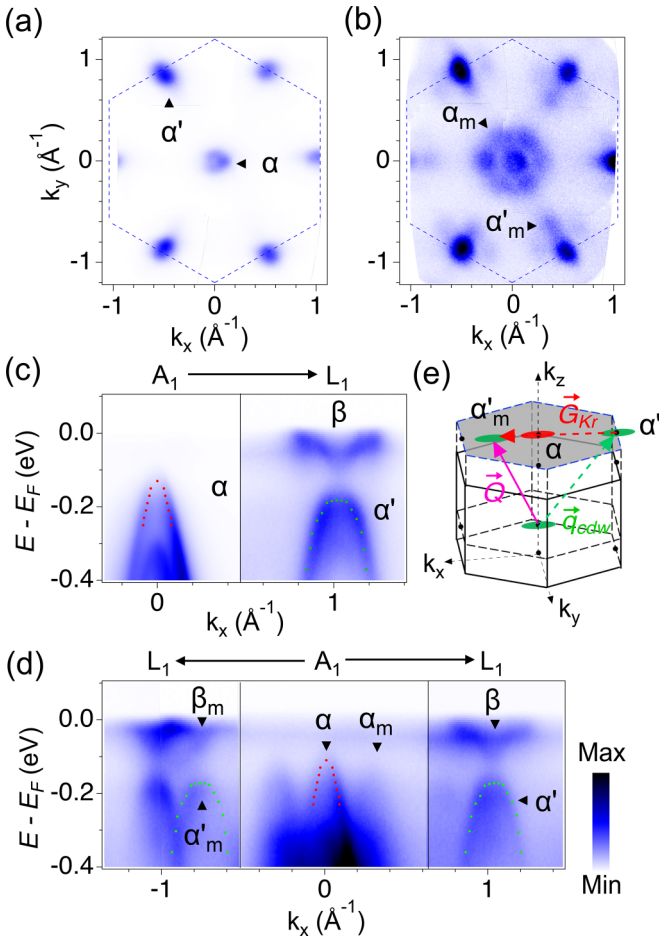


FIG. 2. Interfacial moiré effect in TiSe_2/mKr . (a), (b) The constant energy map at $E_B = 0.17$ eV and band structure along $A_1 - L_1$ direction of pristine TiSe_2 , respectively. (c), (d) Same as (a) and (b), but for TiSe_2/mKr with annealing temperature $T_a = 41$ K. The dots are extracted band dispersions. (e) The schematic interplay between 2D interfacial moiré effect and 3D CDW order in TiSe_2/mKr .

in FS (band-structure) spectra differences between pristine $\text{Cu}_{0.08}\text{TiSe}_2$ and $\text{Cu}_{0.08}\text{TiSe}_2/\text{mKr}$ in Figs. 1(i) and 1(j). As illustrated by Fig. 1(d), the α_m bands are the moiré replicas, by scattering the α band in the second Brillouin zone (BZ) with the reciprocal lattice vector of Kr monolayer (\vec{G}_{Kr}). The distance between the α and α_m in the first BZ is the moiré reciprocal lattice vector ($\vec{G}_m = \vec{G}_{\text{Cu}_{0.08}\text{TiSe}_2} - \vec{G}_{\text{Kr}}$), corresponding to a moiré period of 24.2 \AA . Similarly, the β_m band is the moiré replica by scattering the β band at the opposite edge with \vec{G}_{Kr} .

Our results in Fig. 1 unambiguously demonstrate that the interfacial moiré pattern modulates 3D bulk bands in $\text{Cu}_x\text{TiSe}_2/\text{mKr}$. To further study the interplay between the moiré pattern and CDW ordering, we grow Kr monolayer on TiSe_2 (TiSe_2/mKr) and comprehensively study the effect on electronic structures. The band structure of Kr film confirms the number of gas layers. In Figs. 2(a) and 2(c), we plot a constant-energy map at $E_B = 0.17$ eV and band structure along the $A_1 - L_1$ direction of TiSe_2 in the CDW phase, respectively. Compared to results of $\text{Cu}_{0.08}\text{TiSe}_2$ in Figs. 1(e) and 1(f), CDW folded bands α' appear at the L_1 points in

TiSe_2 . Note that TiSe_2 hosts a 3D CDW order with an out-of-plane vector of $\vec{q}_{\text{CDW}} = (\frac{1}{2}, \frac{1}{2}, \frac{1}{2})$. Therefore, the α' band is folded from the $\Gamma_1 - M_1$ plane (k_z with an offset of π from the $A_1 - L_1$ plane), with a band top slightly lower than that of the α band [Fig. 2(c)] due to the 3D CDW in TiSe_2 . This observation is consistent with previous works [43,44]. As discussed in Supplemental Material, Fig. S3, FS of TiSe_2 also shows intrinsic $C_3 C_3$ symmetry, demonstrating its bulk origin.

We directly observe the interaction between the interfacial moiré effect and 3D CDW in TiSe_2 . By capping a monolayer Kr on TiSe_2 , we observe moiré bulk-band replicas α_m and β_m in TiSe_2/mKr [Figs. 2(b)–2(d)], with the locations and mechanism consistent with those in $\text{Cu}_x\text{TiSe}_2/\text{mKr}$ [Figs. 1(g) and 1(h)]. Furthermore, the CDW folded band α' is also duplicated by the interfacial moiré pattern, resulting in the α'_m band observed right below the β_m band [Fig. 2(d)]. The α'_m replica has the same band top and dispersion as the folded α' band, distinct from the α band and its replica α_m . The observation of the interplay between CDW order and interfacial moiré pattern in TiSe_2/mKr is summarized in Fig. 2(e). The coexistence of 3D CDW and 2D interfacial moiré pattern induces the α'_m replica, by scattering the original α' band in the k'_z plane with a total wave vector of $\vec{Q} = \vec{q}_{\text{CDW}} + \vec{G}_{\text{Kr}}$.

We can further *in situ* tune the moiré pattern. By choosing different noble gases, we manage to achieve the interfacial moiré pattern with moiré period a_m in a large range. For heavier noble gas with bigger atom radius, the lattice constant of the xenon (Xe) monolayer ($a_{\text{Xe}} \sim 4.36 \text{ \AA}$) is larger than the krypton monolayer ($a_{\text{Kr}} \sim 4.02 \text{ \AA}$) and bulk TiSe_2 . Correspondingly, $\text{TiSe}_2/\text{monolayer Xe}$ heterostructure (TiSe_2/mXe) has a smaller moiré period ($a_m^{\text{Xe}} = 15.8 \sim \text{ \AA}$) than that of TiSe_2/mKr ($a_m^{\text{Kr}} = 21.7 \text{ \AA}$) in Fig. 3(b), as evidenced by the largest $\vec{G}_m^{\text{Xe}} = 0.46 \text{ \AA}^{-1}$ observed in TiSe_2/mXe in Fig. 3(a). For the same reason, $\text{TiSe}_2/\text{monolayer Ar}$ heterostructure (TiSe_2/mAr) has the biggest moiré period of $a_m^{\text{Ar}} = 47.1 \text{ \AA}$, as evidenced by the smallest $\vec{G}_m^{\text{Ar}} = 0.15 \text{ \AA}^{-1}$ observed in TiSe_2/mAr in Fig. 3(c). We notice nondispersive spectral intensity near E_F in Figs. 3(a) and 3(b), which is weak and also observed in pristine TiSe_2 (Fig. S4 in the Supplemental Material [37], and [45]). We attribute this feature to the inelastic scattering of the conduction β band by surface disorders.

We can also tune the interfacial moiré pattern *in situ* by annealing processes. Because intralayer interaction in noble-gas monolayer and interlayer interaction between noble-gas monolayer and TiSe_2 are both of the van der Waals type and have comparable interaction strength, the lattice constant of noble-gas monolayer becomes bigger with higher annealing temperature (T_a). This results in a bigger \vec{G}_m as observed in Fig. 3(e), corresponding to a smaller a_m in TiSe_2/mKr with higher T_a . Similar T_a -dependent moiré patterns are observed in TiSe_2/mAr and TiSe_2/mXe (Fig. S5 in the Supplemental Material [37]). As summarized in Fig. 3(f), we can tune the $\text{TiSe}_2/\text{monolayer noble-gas}$ heterostructure with moiré period a_m covering a range from 15.8 to 47.1 \AA . Band-fitting analysis shows signatures of effective mass enhancements in TiSe_2/mAr with a large moiré period a_m , indicative of the moiré-induced band hybridizations (seen in Fig. 5).

We clearly exclude the photoelectron diffraction scenario [46] for the observation of bulk-state replicas, therefore, demonstrating that the interfacial moiré potential modulates

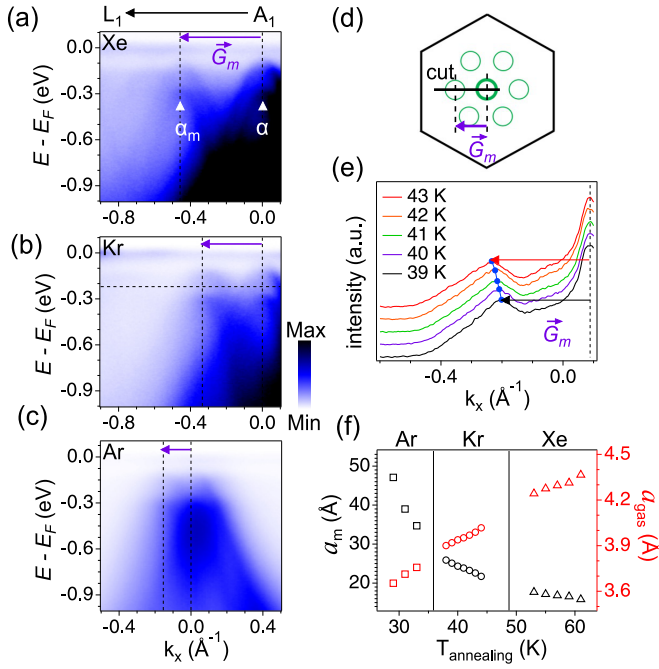


FIG. 3. Control the interfacial moiré period. (a)–(c) Band structures of TiSe_2/mXe with annealing temperature $T_a = 55$ K, TiSe_2/mKr with annealing temperature $T_a = 41$ K and TiSe_2/mAr with annealing temperature $T_a = 31$ K, respectively. (d) The sketch map depicting the replicas. (e) T_a -dependent MDC of TiSe_2/mKr at $E_B = 0.22$ eV, as labeled in (b). (f) T_a -dependent moiré period a_m and lattice constant of noble-gas monolayer in $\text{TiSe}_2/\text{noble-gas}$ monolayer heterostructures.

the initial state. In the final-state diffraction picture, the photoelectrons emitted from TiSe_2 samples can be diffracted by Xe monolayer and induce replicas [Fig. 4(a)]. The photoelectrons' momentum parallel to the surface changes with $\vec{K}_{D\parallel} = \vec{K}_{\parallel} + \vec{G}_{\text{Xe}}$, where \vec{K}_{\parallel} and $\vec{K}_{D\parallel}$ are momentum parallel to the surface before and after diffraction [Fig. 4(b)]. Due to the momentum conservation law, photoelectrons emitted from TiSe_2 samples have a clear detectable momentum cutoff $|\vec{k}_{\parallel}| = |\vec{K}_{\parallel}| \leq \frac{\sqrt{2m_e E_{\text{kin}}}}{\hbar}$, where E_{kin} is photoelectrons' kinetic energy and m_e is free-electron mass. Therefore, the spectra of replicas induced by photoelectron diffraction also have a clear momentum cutoff, because the photoelectrons corresponding to the missing part cannot be emitted from TiSe_2 , thus cannot be diffracted by Xe monolayer subsequently [Figs. 4(b) and 4(c)]. On the other hand, in the case of moiré systems like graphene on BN [47] and other twisted superlattices [2–10], initial states are directly modulated by moiré pattern with replicas hosted [Fig. 4(d)]. Therefore, although the original bands in the high BZs have the spectra cutoff, the replicas sitting within the momentum limitation do not have the cutoff [Figs. 4(e) and 4(f)]. The clear observation of replica bands out of the momentum-cutoff limit excludes the photoelectron diffraction scenario as the reason for the observed bulk-state replicas in TiSe_2/mXe [Fig. 4(g)].

The semimetallic nature of Cu_xTiSe_2 can be critical for the interfacial moiré potential to modulate the bulk states of TMD. We synthesize heterostructures by depositing noble-gas monolayer on metallic TMD NbSe_2 and semiconducting

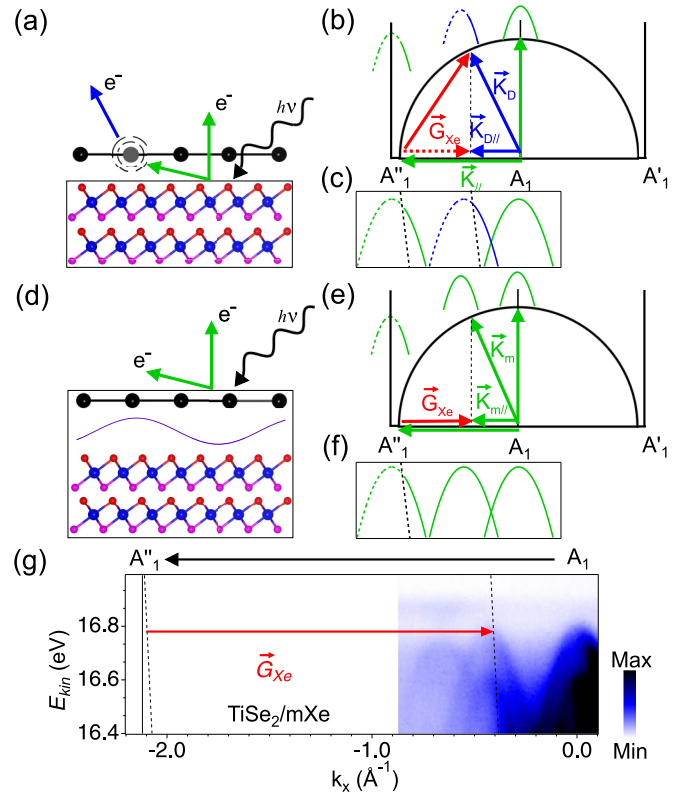


FIG. 4. Origin of the moiré replicas. (a) The illustration of photoelectron diffraction scenario in the real space. The green arrows indicate photoelectrons directly emitted from TiSe_2 . The blue one indicates photoelectrons diffracted by noble-gas monolayer. (b) Same as (a), but in the reciprocal space. The radius of the Ewald sphere (black semicircle) corresponds to the magnitude of the detectable momentum cutoff. The black lines A_1 and A'_1/A'_1 are the center of the first-surface Brillouin zone and the second-surface Brillouin zone of TiSe_2 , respectively. The photoelectrons emitted from the TiSe_2 sample are diffracted on Ewald sphere with $\vec{K}_{D\parallel} = \vec{K}_{\parallel} + \vec{G}_{\text{Xe}}$, where \vec{K}_{\parallel} (green arrow) and $\vec{K}_{D\parallel}$ (blue arrow) are the parallel vectors of photoelectron before and after diffraction, respectively, and \vec{G}_{Xe} (red arrow) is reciprocal lattice vector of Xe monolayer. (c) The illustration of spectra origin from photoelectrons with (blue) and without (green) diffraction. The black dashed lines are momentum cutoffs for the spectra weight. (d)–(f) Same as (a)–(c), but for the scenario of moiré modulation effect on the initial state. (g) The ARPES spectra of TiSe_2/mXe with $T_a = 55$ K.

TMD WSe_2 (Fig. S6). In both cases, the moiré modulation-effect induced bulk-band replicas are absent, as seen in the Supplemental Material, Fig. S6. The screening effect in NbSe_2 is large due to the big carrier concentration, which makes interfacial moiré potential exponentially decrease in bulk. For WSe_2 , the interaction is weak at the interface between two insulating materials. For $\text{Cu}_x\text{TiSe}_2/\text{monolayer}$ noble-gas heterostructure, the interfacial interaction is relatively strong, similar to that in graphite (graphene)/BN [24,25], graphene/monolayer Xe heterostructures [20], and RbV_3Sb_5 polar surface with vacancy filled by noble gas [48]. At the same time, the screening effect is weak due to the semimetallic nature, consistent with the mixed-dimensional moiré potential in graphite-based heterostructures [24,25].

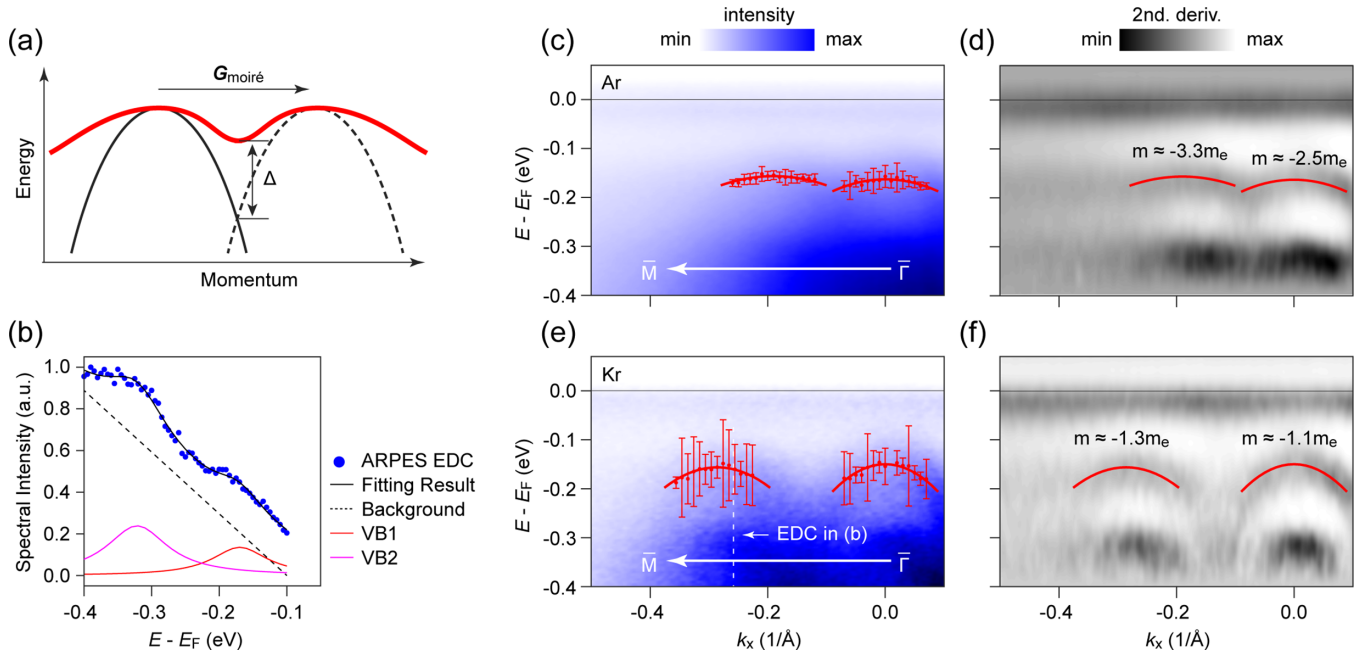


FIG. 5. (a) The schematic diagram of the interaction between the original band (the solid black curve) and the moiré band (the dashed black curve). The interaction can result in a hybridization gap and a band with enhanced effective mass, as indicated by the red curve. (b) The fitting result of a typical energy-distribution curve, as indicated in (e). (c), (e) The ARPES measurement about TiSe_2/mAr (c) and TiSe_2/mKr (e) with the fitted valence-band dispersion appended. The error bars represent the 95% confidence interval from the fitting. (d), (f) The second derivative of (c) and (e), respectively. The fitted parabolas of the band dispersions are appended in (c)–(f) and the corresponding effective masses are indicated.

Three-dimensional CDW orders might be another important factor for the mixed-dimensional moiré effect, as no bulk replica band is observed in the case of monolayer noble gas on the (111) surface of a typical semimetal Bi single crystal (Fig. S6 in the Supplemental Material [37]). Our *ab initio* simulation of TiSe_2/mXe indicates that the 3D CDW can enhance the spectral intensity of the moiré replica of the bulk bands in Fig. 6, which is also manifested by enhanced interfacial coupling between the 3D CDW order and moiré modulation in the real space (Fig. S7 in the Supplemental Material [37]). In contrast, a magnetic field effectively enhances the interlayer coupling in graphite-based mixed-dimensional moiré heterostructures [24,25]. The absence of replica bands in noble-gas monolayer on NbSe_2 , WSe_2 , and Bi(111) surface suggests the intrinsic moiré modulation on initial states in Cu_xTiSe_2 -based heterostructures, as the photoelectron diffraction effect due to the deposited noble-gas monolayer would be universally hosted in these heterostructures and does not depend on substrates.

IV. CONCLUSIONS

In summary, we have shown that noble-gas monolayer deposited on Cu_xTiSe_2 crystal can generate interfacial moiré potentials, which can further strongly modulate the 3D bulk states of Cu_xTiSe_2 . The interfacial moiré superlattice can be *in situ* tuned with the moiré period by more than 3 times. Our results extend the 2D-3D mixed-dimensional moiré heterostructure from graphite systems [24,25] to TMD-based heterostructure. Remarkably, the mixed-dimensional moiré

potential strongly couples with the 3D CDW order in TiSe_2 . The 3D CDW orders in Cu_xTiSe_2 result in strong interlayer interaction with phase matching, which hybridizes the interfacial moiré potential with the Cu_xTiSe_2 bulk states. A previous study suggested that the moiré effect can enhance CDW critical temperature T_{CDW} in 2D limit [11]. Our work provides a promising platform to examine the moiré enhancement on CDW in the 3D case. To synthesize the $\text{Cu}_x\text{TiSe}_2/\text{noble-gas}$ monolayer heterostructure above $T_{\text{CDW}} \sim 200$ K in TiSe_2 , the noble-gas pressure of more than 10^{-5} mbar is needed according to the phase diagram [49], which is too high for ARPES measurements but feasible for other experimental probes such as x-ray diffraction. We observe signatures of effective mass enhancement induced by moiré hybridization with large a_m . Our work motivates further experiments on $\text{Cu}_x\text{TiSe}_2/\text{mAr}$ with higher resolution and lower temperature, to quantitatively analyze the moiré band interactions, and consequently enhanced density of states and correlation effect on superconductivity. Finally, mixed-dimensional moiré potential could also be realized in other CDW crystals or materials with strong interlayer interaction and phase locking.

ACKNOWLEDGMENTS

We thank Shengjun Yuan, Fengcheng Wu, and Zewen Wu for useful discussions. We acknowledge support from the National Natural Science Foundation of China (NSFC) (Grants No. 12274329, No. 12104304, and No. 12304217), Hubei Provincial Natural Science Foundation of China (Grant No. 2024AFB935), the Fundamental Research Funds

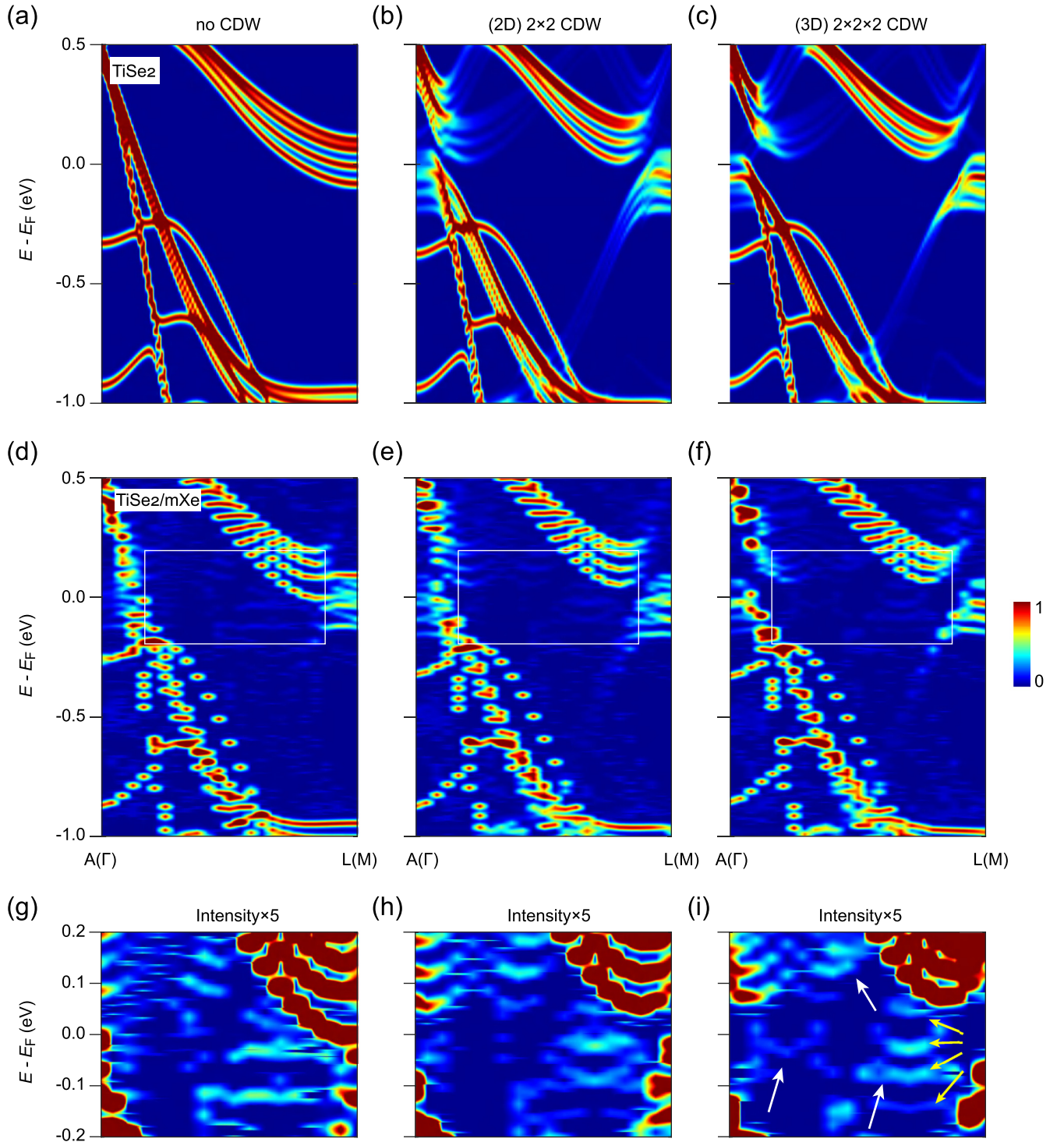


FIG. 6. (a)–(c) The calculated band structures of 4-layer slab TiSe_2 without CDW (a), with the in-plane 2×2 CDW (b), and with the 3D $2 \times 2 \times 2$ CDW (c). (d)–(f) The calculated band structures of monolayer Xe on 4-layer slab TiSe_2 without CDW (d), with the in-plane 2×2 CDW (e), and with the 3D $2 \times 2 \times 2$ CDW (f). (g)–(i) Zoom-in plot of (d)–(f) in the momentum-energy area indicated by the white rectangles, with 5 times enhanced intensity.

for the Central Universities (Grant No. 2042023kf0107), and the China Postdoctoral Science Foundation (Grant No. 2023M732717). Y.X. acknowledges support from the Innovation Program for Quantum Science and Technology (Grant No. 2021ZD0302802) and Anhui University through the start-up project (Project No. S020318001/020).

APPENDIX A: THE EFFECTIVE MASSES OF THE MOIRÉ REPLICAS BANDS IN TiSe_2/mKr AND TiSe_2/mAr

We extracted the effective masses of the moiré replica bands in TiSe_2/mKr and TiSe_2/mAr , as shown in Figs. 5(c)–5(f) by careful analysis on the ARPES measurement of

energy-distribution-curves. Figure 5(b) shows a fitting result of a typical energy-distribution curve, which consists of Lorentzian profiles of valence bands and a linear background. We obtained the effective masses by fitting the valence-band dispersions to parabolas, as shown in Figs. 5(c) and 5(e). As the moiré superlattice becomes larger (the reciprocal vector of the moiré period \vec{G}_m becomes smaller), the effective mass of the moiré replica band increases, as presented in Figs. 5(d) and 5(f). This observation is consistent with our previous study on graphene/mXe [20], in which the moiré band became nearly flat for large moiré periods. The flattening of the moiré replica bands is an indication of the expected interaction between moiré bands.

APPENDIX B: THE BAND STRUCTURE CALCULATIONS TO SIMULATE THE EFFECT OF THE CDW IN TiSe₂ ON THE 3D BULK REPLICAS IN TiSe₂/mXe

We carry out the first-principles calculations in the framework of the generalized gradient approximation functional [50] of the density-functional theory with projector augmented-wave method [51] implemented in the Vienna *Ab initio* Simulation Package (VASP) [52]. In all calculations, we use the slab model of Xe monolayer and 4-layer TiSe₂ to study the moiré effect. The structures are fully optimized until all the Hellmann-Feynman forces on each atom are

less than $0.01 \text{ eV } \text{Å}^{-1}$ and the total energy difference between two successive steps is smaller than 10^{-6} eV . Then we perform the band-unfolding calculation with the help of VASPKIT code [VASPKIT: A user-friendly interface facilitating high-throughput computing and analysis using VASP code].

To reveal the influence of CDW on the system, we compared the band structures along the *A-L* direction of TiSe₂ with a 4-layer slab without CDW, with in-plane 2×2 CDW, and with 3D $2 \times 2 \times 2$ CDW, as shown in Figs. 6(a)–6(c), respectively. The valence- and conduction bands split into 4 branches, which originate from 4 layers due to the interlayer coupling. The Xe monolayer on top of the 4-layer TiSe₂ slab introduces the moiré modulation and creates moiré replica bands, as shown in Figs. 6(d)–6(f). The moiré replica bands are the most pronounced and coherent in the 3D $2 \times 2 \times 2$ CDW model, as shown in Figs. 6(f) and 6(i). The moiré replica of the valence- and conduction bands can be clearly seen in the area near E_F along the *A-L* direction, as marked by the arrows in the zoom-in plot [Fig. 6(i)]. One can notice that the moiré replica bands also split into 4 branches, as marked by the yellow arrows in Fig. 6(i), indicating that the moiré modulation is not localized on the top layer but extended through the whole 4-layer slab. Despite a simplified model, our simulated calculation results indicate that the 3D CDW can significantly enhance the spectral intensity of the moiré replica of the bulk bands, which supports our experimental observations.

-
- [1] A. K. Geim and I. V. Grigorieva, Van der Waals heterostructures, *Nature (London)* **499**, 419 (2013).
- [2] Y. Cao, V. Fatemi, S. A. Fang, K. Watanabe, T. Taniguchi, E. Kaxiras, and P. Jarillo-Herrero, Unconventional superconductivity in magic-angle graphene superlattices, *Nature (London)* **556**, 43 (2018).
- [3] Y. Cao, V. Fatemi, A. Demir, S. A. Fang, S. L. Tomarken, J. Y. Luo, J. D. Sanchez-Yamagishi, K. Watanabe, T. Taniguchi, E. Kaxiras, R. C. Ashoori, and P. Jarillo-Herrero, Correlated insulator behaviour at half-filling in magic-angle graphene superlattices, *Nature (London)* **556**, 80 (2018).
- [4] Y. Cao, D. Rodan-Legrain, O. Rubies-Bigorda, J. M. Park, K. Watanabe, T. Taniguchi, and P. Jarillo-Herrero, Tunable correlated states and spin-polarized phases in twisted bilayer-bilayer graphene, *Nature (London)* **583**, 215 (2020).
- [5] K. Tran, G. Moody, F. Wu, X. Lu, J. Choi, K. Kim, A. Rai, D. A. Sanchez, J. Quan, A. Singh, J. Embley, A. Zepeda, M. Campbell, T. Autry, T. Taniguchi, K. Watanabe, N. Lu, S. K. Banerjee, K. L. Silverman *et al.*, Evidence for moiré excitons in van der Waals heterostructures, *Nature (London)* **567**, 71 (2019).
- [6] E. Y. Andrei and A. H. MacDonald, Graphene bilayers with a twist, *Nat. Mater.* **19**, 1265 (2020).
- [7] L. Balents, C. R. Dean, D. K. Efetov, and A. F. Young, Superconductivity and strong correlations in moiré flat bands, *Nat. Phys.* **16**, 725 (2020).
- [8] M. Serlin, C. L. Tschirhart, H. Polshyn, Y. Zhang, J. Zhu, K. Watanabe, T. Taniguchi, L. Balents, and A. F. Young, Intrinsic quantized anomalous Hall effect in a moiré heterostructure, *Science* **367**, 900 (2020).
- [9] S. W. Chen, M. H. He, Y. H. Zhang, V. Hsieh, Z. Y. Fei, K. Watanabe, T. Taniguchi, D. H. Cobden, X. D. Xu, C. R. Dean, and M. Yankowitz, Electrically tunable correlated and topological states in twisted monolayer-bilayer graphene, *Nat. Phys.* **17**, 374 (2021).
- [10] G. R. Chen, A. L. Sharpe, E. J. Fox, Y. H. Zhang, S. X. Wang, L. L. Jiang, B. Lyu, H. Y. Li, K. Watanabe, T. Taniguchi, Z. W. Shi, T. Senthil, D. Goldhaber-Gordon, and Y. B. Zhang, Tunable correlated Chern insulator and ferromagnetism in a moiré superlattice, *Nature (London)* **579**, 56 (2020).
- [11] W. Zhao, L. Zhu, Z. Nie, Q. Li, Q. Wang, L. Dou, J. Hu, L. Xian, S. Meng, and S.-C. Li, Moiré enhanced charge density wave state in twisted 1T-TiTe₂/1T-TiSe₂ heterostructures, *Nat. Mater.* **21**, 284 (2022).
- [12] C. Jin, E. C. Regan, A. Yan, M. Iqbal Bakti Utama, D. Wang, S. Zhao, Y. Qin, S. Yang, Z. Zheng, S. Shi, K. Watanabe, T. taniguchi, S. Tongay, A. Zettl, and F. Wang, Observation of moiré excitons in WSe₂/WS₂ heterostructure superlattices, *Nature (London)* **567**, 76 (2019).
- [13] Y. Tang, L. Li, T. Li, Y. Xu, S. Liu, K. Barmak, K. Watanabe, T. Taniguchi, A. H. MacDonald, J. Shan, and K. F. Mak, Simulation of Hubbard model physics in WSe₂/WS₂ moiré superlattices, *Nature (London)* **579**, 353 (2020).
- [14] H. Li, S. Li, M. H. Naik, J. Xie, X. Li, J. Wang, E. Regan, D. Wang, W. Zhao, S. Zhao, S. Kahn, K. Yumigeta, M. Blei, T. Taniguchi, K. Watanabe, S. Tongay, A. Zettl, S. G. Louie, F. Wang, and M. F. Crommie, Imaging moiré flat bands in three-dimensional reconstructed WSe₂/WS₂ superlattices, *Nat. Mater.* **20**, 945 (2021).

- [15] E. Liu, E. Barré, J. van Baren, M. Wilson, T. Taniguchi, K. Watanabe, Y. Cui, N. M. Gabor, T. F. Heinz, Y. Chang, and C. H. Lui, Signatures of moiré trions in $\text{WSe}_2/\text{MoSe}_2$ heterobilayers, *Nature (London)* **594**, 46 (2021).
- [16] Y. Shimazaki, I. Schwartz, K. Watanabe, T. Taniguchi, M. Kroner, and A. Imamoglu, Strongly correlated electrons and hybrid excitons in a moiré heterostructure, *Nature (London)* **580**, 472 (2020).
- [17] L. Ma, P. X. Nguyen, Z. Wang, Y. Zeng, K. Watanabe, T. Taniguchi, A. H. MacDonald, K. F. Mak, and J. Shan, Strongly correlated excitonic insulator in atomic double layers, *Nature (London)* **598**, 585 (2021).
- [18] K. Schouteden, Z. Li, T. S. Chen, F. Q. Song, B. Partoens, C. Van Haesendonck, and K. Park, Moiré superlattices at the topological insulator Bi_2Te_3 , *Sci. Rep.* **6**, 20278 (2016).
- [19] C. L. Wu, Q. Wan, C. Peng, S. K. Mo, R. Z. Li, K. M. Zhao, Y. P. Guo, D. Huo, C. D. Zhang, and N. Xu, Observation of high-order moiré effect and multiple Dirac fermions replicas in graphene-SiC heterostructures, *Phys. Rev. B* **104**, 235130 (2021).
- [20] C. L. Wu, Q. Wan, C. Peng, S. K. Mo, R. Z. Li, K. M. Zhao, Y. P. Guo, S. J. Yuan, F. C. Wu, C. D. Zhang, and N. Xu, Tailoring Dirac fermions by *in-situ* tunable high-order moiré pattern in graphene-monolayer xenon heterostructure, *Phys. Rev. Lett.* **129**, 176402 (2022).
- [21] Y. W. Li, Q. Wan, and N. Xu, Recent advances in moiré superlattice systems by angle-resolved photoemission spectroscopy, *Adv. Mater.* **2305175** (2023).
- [22] S. Im, H. Im, K. Kim, J.-E. Lee, J. Hwang, S.-K. Mo, and C. Hwang, Modified Dirac fermions in the crystalline xenon and graphene moiré heterostructure, *Adv. Phys. Res.* **2**, 2200091 (2023).
- [23] Q. Wan, C. Wu, X.-J. Luo, S. Dai, C. Peng, R. Li, S. Mo, K. Zhao, W.-X. Qiu, H. Zhong, Y. Li, C. Zhang, F. Wu, and N. Xu, Quantum simulation of a honeycomb lattice model by high-order moiré pattern, *Phys. Rev. B* **109**, L161102 (2024).
- [24] D. Waters, E. Thompson, E. Arreguin-Martinez, M. Fujimoto, Y. Ren, K. Watanabe, T. Taniguchi, T. Cao, D. Xiao, and M. Yankowitz, Mixed-dimensional moiré systems of twisted graphitic thin films, *Nature (London)* **620**, 750 (2023).
- [25] C. Mullan, S. Slizovskiy, J. Yin, Z. Wang, Q. Yang, S. Xu, Y. Yang, B. A. Piot, S. Hu, T. Taniguchi, K. Watanabe, K. S. Novoselov, A. K. Geim, V. I. Fal'ko, and A. Mishchenko, Mixing of moiré-surface and bulk states in graphite, *Nature (London)* **620**, 756 (2023).
- [26] G. Li, W. Z. Hu, D. Qian, D. Hsieh, M. Z. Hasan, E. Morosan, R. J. Cava, and N. L. Wang, Semimetal-to-semimetal charge density wave transition in 1T-TiSe₂, *Phys. Rev. Lett.* **99**, 027404 (2007).
- [27] F. J. DiSalvo, D. E. Moncton, and J. V. Waszczak, Electronic properties and superlattice formation in the semimetal TiSe₂, *Phys. Rev. B* **14**, 4321 (1976).
- [28] C. Monney, C. Battaglia, H. Cercellier, P. Aebi, and H. Beck, Exciton condensation driving the periodic lattice distortion of 1T-TiSe₂, *Phys. Rev. Lett.* **106**, 106404 (2011).
- [29] A. Kogar, M. S. Rak, S. Vig, A. A. Husain, F. Flicker, Y. Il Joe, L. Venema, G. J. MacDougall, T. C. Chiang, E. Fradkin, J. van Wezel, and P. Abbamonte, Signatures of exciton condensation in a transition metal dichalcogenide, *Science* **358**, 1314 (2017).
- [30] H. Cercellier, C. Monney, F. Clerc, C. Battaglia, L. Despont, M. G. Garnier, H. Beck, P. Aebi, L. Patthey, H. Berger, and L. Forró, Evidence for an excitonic insulator phase in 1T-TiSe₂, *Phys. Rev. Lett.* **99**, 146403 (2007).
- [31] F. Weber, S. Rosenkranz, J.-P. Castellan, R. Osborn, G. Karapetrov, R. Hott, R. Heid, K.-P. Bohnen, and A. Alatas, Electron-phonon coupling and the soft phonon mode in TiSe₂, *Phys. Rev. Lett.* **107**, 266401 (2011).
- [32] M. Holt, P. Zschack, H. Hong, M. Y. Chou, and T.-C. Chiang, X-ray studies of phonon softening in TiSe₂, *Phys. Rev. Lett.* **86**, 3799 (2001).
- [33] T. E. Kidd, T. Miller, M. Y. Chou, and T.-C. Chiang, Electron-hole coupling and the charge density wave transition in TiSe₂, *Phys. Rev. Lett.* **88**, 226402 (2002).
- [34] E. Morosan, H. W. Zandbergen, B. S. Dennis, J. W. G. Bos, Y. Onose, T. Klimczuk, A. P. Ramirez, N. P. Ong, and R. J. Cava, Superconductivity in Cu_xTiSe_2 , *Nat. Phys.* **2**, 544 (2006).
- [35] A. Kogar, G. A. de la Pena, Sangjun Lee, Y. Fang, S. X.-L. Sun, D. B. Lioi, G. Karapetrov, K. D. Finkelstein, J. P. C. Ruff, P. Abbamonte, and S. Rosenkranz, Observation of a charge density wave incommensuration near the superconducting dome in Cu_xTiSe_2 , *Phys. Rev. Lett.* **118**, 027002 (2017).
- [36] S. Duan, Y. Cheng, W. Xia, Y. Yang, C. Xu, F. Qi, C. Huang, T. Tang, Y. Guo, W. Luo, D. Qian, D. Xiang, J. Zhang, and W. Zhang, Optical manipulation of electronic dimensionality in a quantum material, *Nature (London)* **595**, 239 (2021).
- [37] See Supplemental Material at <http://link.aps.org/supplemental/10.1103/PhysRevB.110.085148> for the photoemission data about noble gas on TiSe₂, LEED pattern of the $\text{Cu}_{0.08}\text{TiSe}_2/\text{mXe}$; the 3D bulk states exhibiting C_3 symmetry pattern before and after depositing Kr monolayer on TiSe₂; the band dispersion of TiSe_2/mXe and pristine TiSe₂; the band dispersion of Ar, Kr, and Xe monolayer on TiSe₂; the band structures of noble gas monolayers on NbSe₂, WSe₂, and Bi(111); the real-space moiré superlattice calculations simulate the effect of CDW on the moiré superlattice, which includes Refs. [20,38–40,45].
- [38] T. Mandel, G. Kaindl, M. Demke, W. Fischer, and W. D. Schneider, Layer-by-layer band structure of physisorbed Xe on Al (111), *Phys. Rev. Lett.* **55**, 1638 (1985).
- [39] K. Hermann, J. Noffke, and K. Horn, Lateral interactions in rare gas monolayers: Band-structure models and photoemission experiments, *Phys. Rev. B* **22**, 1022 (1980).
- [40] T. Mandel, M. Domke, and G. Kaindl, Layer-resolved band dispersion of rare-gas multilayers on graphite (001), *Surface Sci.* **197**, 81 (1988).
- [41] J. F. Zhao, H. W. Ou, G. Wu, B. P. Xie, Y. Zhang, D. W. Shen, J. Wei, L. X. Yang, J. K. Dong, M. Arita, H. Namatame, M. Taniguchi, X. H. Chen, and D. L. Feng, Evolution of the electronic structure of 1T-Cu_xTiSe₂, *Phys. Rev. Lett.* **99**, 146401 (2007).
- [42] D. Qian, D. Hsieh, L. Wray, E. Morosan, N. L. Wang, Y. Xia, R. J. Cava, and M. Z. Hasan, Emergence of Fermi pockets in a new excitonic charge-density-wave melted superconductor, *Phys. Rev. Lett.* **98**, 117007 (2007).
- [43] M. D. Watson, O. J. Clark, F. Mazzola, I. Marković, V. Sunko, T. K. Kim, K. Rossnagel, and P. D. C. King, Orbital- and kz-selective hybridization of Se 4p and Ti 3d states in the charge density wave phase of TiSe₂, *Phys. Rev. Lett.* **122**, 076404 (2019).

- [44] P. Chen, Y.-H. Chan, X.-Y. Fang, Y. Zhang, M. Y. Chou, S.-K. Mo, Z. Hussain, A.-V. Fedorov, and T.-C. Chiang, Charge density wave transition in single-layer titanium diselenide, *Nat. Commun.* **6**, 8943 (2015).
- [45] M. M. May, C. Brabetz, C. Janowitz, and R. Manzke, Charge-density-wave phase of 1T-TiSe₂: The influence of conduction band population, *Phys. Rev. Lett.* **107**, 176405 (2011).
- [46] C. M. Polley, L. I. Johansson, H. Fedderwitz, T. Balasubramanian, M. Leandersson, J. Adell, R. Yakimova, and C. Jacobi, Origin of the π -band replicas in the electronic structure of graphene grown on 4H-SiC (0001), *Phys. Rev. B* **99**, 115404 (2019).
- [47] E. Wang, X. Lu, S. Ding, W. Yao, M. Yan, G. Wan, K. Deng, S. Wang, G. Chen, L. Ma, J. Jung, A. V. Fedorov, Y. Zhang, G. Zhang, and S. Zhou, Gaps induced by inversion symmetry breaking and second-generation Dirac cones in graphene/hexagonal boron nitride, *Nat. Phys.* **12**, 1111 (2016).
- [48] C. Peng, Y. Li, X. Chen, S. Dai, Z. Wu, C. Wu, Q. Wan, K. Zhao, R. Li, S. Mo, D. Qin, S. Yu, H. Zhong, S. Yuan, J. Guo, and N. Xu, Surface region band enhancement in noble-gas adsorption assisted angle-resolved photoemission spectroscopy on the kagome superconductor RbV₃Sb₅, *Phys. Rev. B* **109**, 115415 (2024).
- [49] P. S. Schabes-Retchkiman and J. A. Venables, Structural studies of xenon and krypton solid monolayers on graphite using transmission electron diffraction, *Surf. Sci.* **105**, 536 (1981).
- [50] J. P. Perdew, K. Burke, and M. Ernzerhof, Generalized gradient approximation made simple, *Phys. Rev. Lett.* **77**, 3865 (1996).
- [51] P. E. Blöchl, Projector augmented-wave method, *Phys. Rev. B* **50**, 17953 (1994).
- [52] G. Kresse and J. Hafner, Ab initio molecular dynamics for liquid metals, *Phys. Rev. B* **47**, 558 (1993).